Optical/UV-to-X-Ray Echoes from the Tidal Disruption Flare ASASSN-14li

Dheeraj R. Pasham[1,8], S. Bradley Cenko[2,3], Aleksander Sadowski[1,8], James Guillochon[4,9], Nicholas C. Stone[5,8],
Sjoert van Velzen[6,10], and John K. Cannizzo[2,7]

[1] Massachusetts Institute of Technology, Cambridge, MA 02139, USA
[2] NASA's Goddard Space Flight Center, Greenbelt, MD 20771, USA
[3] Joint Space-Science Institute, University of Maryland, College Park, MD 20742, USA
[4] Harvard-Smithsonian Center for Astrophysics, Cambridge, MA 02138, USA
[5] Columbia University, New York, NY 10027, USA
[6] The Johns Hopkins University, Baltimore, MD 21218, USA
[7] Department of Physics, University of Maryland, Baltimore County, Baltimore, MD 21250, USA

Abstract

We carried out the first multi-wavelength (optical/UV and X-ray) photometric reverberation mapping of a tidal disruption flare (TDF) ASASSN-14li. We find that its X-ray variations are correlated with and lag the optical/UV fluctuations by 32 ± 4 days. Based on the direction and the magnitude of the X-ray time lag, we rule out X-ray reprocessing and direct emission from a standard circular thin disk as the dominant source of its optical/UV emission. The lag magnitude also rules out an AGN disk-driven instability as the origin of ASASSN-14li and thus strongly supports the tidal disruption picture for this event and similar objects. We suggest that the majority of the optical/UV emission likely originates from debris stream self-interactions. Perturbations at the self-interaction sites produce optical/UV variability and travel down to the black hole where they modulate the X-rays. The time lag between the optical/UV and the X-rays variations thus correspond to the time taken by these fluctuations to travel from the self-interaction site to close to the black hole. We further discuss these time lags within the context of the three variants of the self-interaction model. High-cadence monitoring observations of future TDFs will be sensitive enough to detect these echoes and would allow us to establish the origin of optical/UV emission in TDFs in general.

Key words: accretion, accretion disks – black hole physics

Supporting material: data behind figure

1. Introduction

When a star comes sufficiently close to a massive black hole ($10^{4-8}~M_\odot$) such that tidal forces exceed its self-gravity, it will be torn apart to cause a stellar tidal disruption flare (TDF; Hills [1975](#); Rees [1988](#)). These events not only have the potential to uncover a large population of hidden massive black holes but could also enable us to understand how jets are launched and disks are formed.

One of the recent controversies about TDFs is, where does the majority of the optical/UV emission originate from in TDFs? (Piran et al. [2015](#) (P15); Roth et al. [2016](#); Dai et al. [2015](#); etc.). In some of the best-studied events, the optical/UV blackbody radius is much larger than the tidal radius, and the temperature remains roughly constant over much of the evolution (e.g., Chornock et al. [2014](#); Holoien et al. [2016b](#)). Because TDFs are basically accreting supermassive black holes, the natural inclination is to expect the same mechanisms operating in AGN, namely, X-ray reprocessing, thermal emission from the inner radii of the accretion disk, etc., to also operate in TDFs. Here, we use publicly available multi-wavelength (optical/UV and X-ray) data from a recent TDF, ASASSN-14li, to constrain the origin of its optical/UV emission.

ASASSN-14li was discovered as an optical transient by the All-Sky Automated Survey for SuperNovae (ASASSN; Shappee et al. [2014](#)) on 2014 November 11 (Holoien et al. [2016a](#), hereafter H16). Based on its spatial coincidence with its host galaxy's nucleus, its peak luminosity of roughly $10^{44}~\mathrm{erg~s^{-1}}$, and its blue optical spectrum with broad and transient Hα and He emission lines, it has been categorized as an event caused by the tidal disruption of a star by a supermassive black hole ([H16](#)). We carried out a photometric reverberation analysis of ASASSN-14li to find that the variations in its X-ray bandpass are correlated with and lag the optical/UV fluctuations by 32 days. We describe the data and our analysis in Sections [2](#) and [3](#) and discuss the implications of our result for the likely origin of the optical/UV emission from this source in Section [4](#).

2. Optical/UV and X-Ray Observations

The multi-wavelength data used in this Letter were acquired from two different facilities: the *Swift* satellite (Gehrels et al. [2004](#)) and the Las Cumbres Observatory Global Telescope (LCOGT) network (Brown et al. [2013](#)). *Swift*'s X-Ray Telescope (XRT; Burrows et al. [2005](#)) provided the X-ray (0.3–10 keV) data, while its UV Optical Telescope (UVOT; Roming et al. [2005](#)) provided the UV data in the UVW2, UVM2, and the UVW1 filters with centroid wavelengths of 1928, 2246, and 2600 Å, respectively (Poole et al. [2008](#)). The UVOT also facilitated optical data in the U, B, and the V bands with centroid wavelengths of 3465, 4392, and 5468 Å, respectively (Poole et al. [2008](#)). However, because the B- and the V-band optical observations were poorly sampled for the second half of *Swift*'s monitoring campaign

---

[8] Einstein Fellow.
[9] Harvard ITC Fellow.
[10] Hubble Fellow.

(see Figure 2 of H16), we also used published LCOGT's g-band optical data (centroid wavelength of 4770 Å). We re-analyzed all of the X-ray and the UVOT data from *Swift*. Our reduction and analysis procedures are described in detail below.

2.1. X-Ray Data Analysis

Swift started monitoring the TDF ASASSN-14li roughly eight days after its discovery on MJD 56983.6 (H16). It observed the source for 1–3 ks roughly once every three days for the first ≈260 days of the campaign. However, after this time the target became Sun-constrained to *Swift* and the monitoring campaign suffered from longer data gaps. Therefore, we limited our analysis to the first 270 days of post-outburst data at all wavelengths.

After extracting the clean eventlists from the raw Level-1 XRT products, we accounted for pile-up (Miller et al. 2015) by extracting X-ray (0.3–10.0 keV) source events from an annular region (rather than a circular region) centered on the source's centroid. As recommended by the XRT data analysis guide,[11] we modeled the PSF in each observation to estimate an inner exclusion radius. The inner exclusion radius of the source extraction region varied between $0''$ and $15''$ while the outer radius was fixed at $50''$. The background count rates were extracted from annuli centered on the source with inner and outer radii of $70''$ and $250''$, respectively. Thus, we extracted a pile-up and background-corrected source count rate from each *Swift* observation. We also corrected for bad pixels following the procedure outlined by the *Swift* data analysis guide.[12] Because ASASSN-14li's X-ray energy spectrum remains roughly constant during the first 250 days of the outburst (see Figure 3 of Miller et al. 2015 and Table S5 of Brown et al. 2017), the count rate serves as a good indicator of its intrinsic flux.

2.2. UVOT Data Analysis

The UVOT (Roming et al. 2005) on board *Swift* began observing ASASSN-14li at 10:08 UT on 2014 November 30. We downloaded the data from the HEASARC archive.[13] In each of the six broadband filters (UVW2, UWM2, UVW1, U, B, and V), we corrected the image astrometry and stacked frames on a per-visit basis.

We performed photometry on the stacked images using a $3''$ aperture and corrected to the standard UVOT photometric system (Poole et al. 2008; Breeveld et al. 2011). To account for contamination from the host underlying a host galaxy, a particularly important contribution to the observed emission in the redder filters, we utilize the coincidence-loss corrected host flux estimates from Miller et al. (2015; see also H16 and van Velzen et al. 2016). All the optical/UV light curves are consistent with H16. The cross-correlation results below are independent of host-subtraction.

3. Cross-correlation Analysis

In order to search for and quantify any correlation between the X-ray and the optical/UV variations, we employed the interpolated cross-correlation function (ICCF) methodology as described by Peterson et al. (2004). We first de-trended the

X-ray light curve with a bending power-law model (red curve in the top left panel of Figure 1). Each of the optical/UV light curves were then de-trended with a power-law decay model. A sample fit for the UVW1 data is shown as a dashed red curve in the top middle panel of Figure 1. The X-ray residual was then cross-correlated with each of the seven optical/UV residuals. A sample ICCF between the X-ray and the UVW1 data is shown in the top right panel of Figure 1, while the rest of the ICCFs are shown in Figures 2 and 3. It is evident that the CCFs peak between 25 and 35 days indicating that the X-ray variations lag the optical/UV fluctuations by 25–35 days.

In order to confirm these CCFs, we also visually inspected them and compared the variability features in the X-ray data with the features in the optical/UV residual light curves. These are shown in the bottom right panel of Figure 1 and the right panels of Figures 2 and 3. In each of these panels, common features in both the light curves are evident. Some of these CCFs also show evidence for an anti-correlation at zero lag. However, we do not consider it to be real as visual inspection of the light curve residuals did not reveal a strong evidence for an anti-correlation.

The X-ray and the lead-corrected optical/UV residual light curves in Figures 1–3 suggest that the correlation functions are driven by three X-ray variability features: two broad peaks (one around day 50 and the second around day 110) and one trough around day 80 in the X-ray data (see the top right panel of Figure 2). Correspondingly, these features are also present in the optical/UV residual light curves but offset by ≈ -32 days (see the top right panel of Figure 2).

In order to estimate the statistical significance of the correlations, we estimated the chance probability that the X-ray light curve would produce these same variability features evident in a given optical/UV light curve. For this purpose, we simulated 10^5 white noise light curves to mimic the X-ray residual light curve. We constructed these synthetic X-ray light curves by drawing from a Gaussian distribution with a mean of zero and a standard deviation equal to the standard deviation of the observed X-ray residual light curve. We then evaluated simulated ICCFs by cross-correlating each of these simulated X-ray residual light curves with each of the optical/UV residual light curves. This way—for each X-ray—optical/UV ICCF—we built a distribution of the 10^5 correlation values at each lag. Using these distributions, we extracted the 95% (blue) and the 99% (magenta) confidence contours shown in the top right panel of Figure 1 (see also Figures 2 and 3). We then estimated the uncertainty in the peak and the centroid of the ICCFs using the Random Subset Selection and the Flux Randomization procedures as described by Peterson et al. (1998, 2004). The resulting cross-correlation centroid and peak distributions for the case of X-ray versus UVW1 ICCF are shown in the bottom left and the bottom middle panels of Figure 1, respectively.

Using the binomial distribution formula, we also estimated the global statistical significance of the X-ray variations lagging the optical/UV fluctuations to be $>4.4\sigma$. This was estimated based on the fact that five out of seven CCFs have the correlation peaks detected at greater than the 95% confidence (see, for example, Pasham et al. 2015 and Tombesi et al. 2010 within the context of timing and spectroscopy, respectively).

We also evaluated all the X-ray–optical/UV CCFs using the discrete cross-correlation function (DCF) algorithm as described by Edelson & Krolik (1988). We find that the
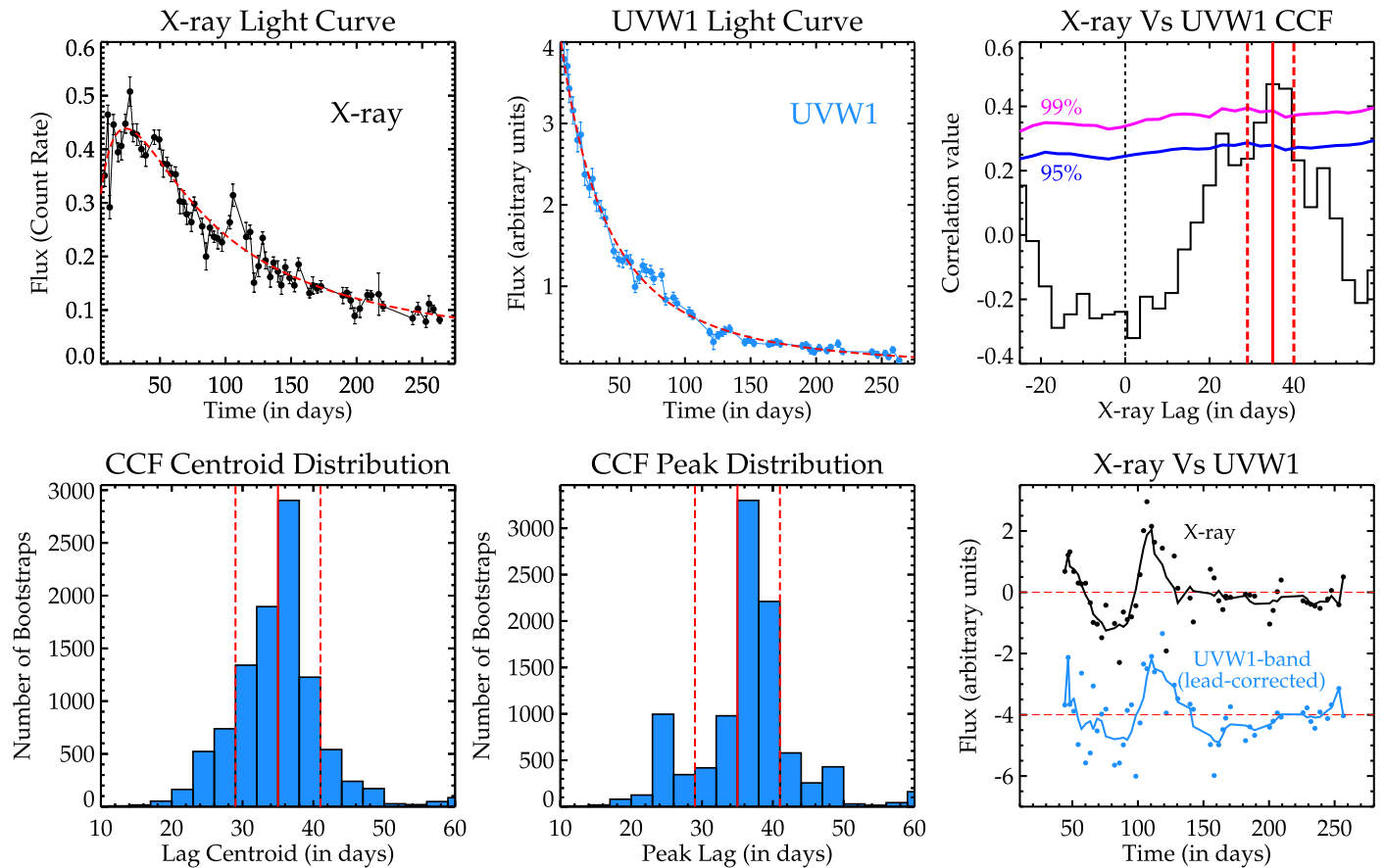
Figure 1. Top left: ASASSN-14li's observed X-ray light curve (black data points) along with the best-fit bending power-law model (dashed red). Top middle: ASASSN-14li's observed UVW1 light curve (blue) along with the best-fit decaying power-law model (dashed red). All the best-fit model parameters can be found in the data behind this figure. Top right: interpolated cross-correlation function (ICCF) between the de-trended X-ray and the UVW1 light curves. The 95% (blue) and the 99% (magenta) white noise statistical confidence contours are also shown. The solid vertical red line is the median of the CCF's centroid distribution (35^{+5}_{-6} days) shown in the bottom left panel. The 1σ error bars are shown as the dashed vertical red lines (same as in the bottom left panel). Bottom middle: ICCF's peak distribution. The solid vertical line is the median while the dashed lines are the 1σ error bars. Bottom right: we compare the variability features in the X-ray and the UVW1 light curves. ASASSN-14li's UVW1 light curve is offset by 35 days (blue). The black data points show the X-ray light curve interpolated at the lead-corrected UVW1 epochs. Both the light curves were de-trended by subtracting a smooth function (top panels), leaving only the variability features. The solid curves are a running average of five neighboring points, to guide the eye. All the X-ray and optical/UV photometric measurements can be found in the data behind this figure. (The data used to create this figure are available.)

resulting DCFs are consistent with the ICCFs shown in Figures 1–3.

Because a CCF is simply a convolution of the autocorrelation function (ACF) with a transfer function, a lag between the X-ray and the optical/UV light curve is real only if it arises from the transfer function and not from the X-ray or the optical/UV ACF. To rule out an ACF origin for the lag we extracted the X-ray and the optical/UV ACFs to find that they do not have any statistically significant lag features except at zero lag.

4. Discussion

First, we demonstrate that the measured optical/UV–X-ray lag in ASASSN-14li implies that none of the three primary mechanisms[14] that can drive X-ray variations to correlate with the optical/UV changes in AGN (e.g., Edelson et al. 2015; McHardy et al. 2016) are at play here.

---
[14] Other mechanisms similar to stellar-mass black hole binaries may also play a role (e.g., Gandhi et al. 2010 and references therein), but on timescales much shorter than observed here.

A. In the first mechanism, X-rays from close to the black hole scatter off material in the outer regions of the accretion disk or any other surrounding medium, lose energy, and get reprocessed into lower-energy optical/ UV photons (Edelson et al. 2015). In this case, the X-ray variations would lead the optical changes by a few days to a few tens of days depending on the distance to the outer disk (Morgan et al. 2010)/reprocessing medium.

B. However, if a significant fraction of the optical/UV emission originates directly from the accretion disk as a thermal blackbody, then two kinds of correlations are possible:

(1) If the majority of the X-rays are produced in a corona that is powered by Compton up-scattering of near-UV seed photons from the thermal inner disk (Reynolds & Nowak 2003), then the X-ray variations would lag the near-UV fluctuations by a fraction of a day to a few days depending on the size of the corona and the inner disk (which are determined by the black hole mass (Arévalo et al. 2005) and accretion rate).
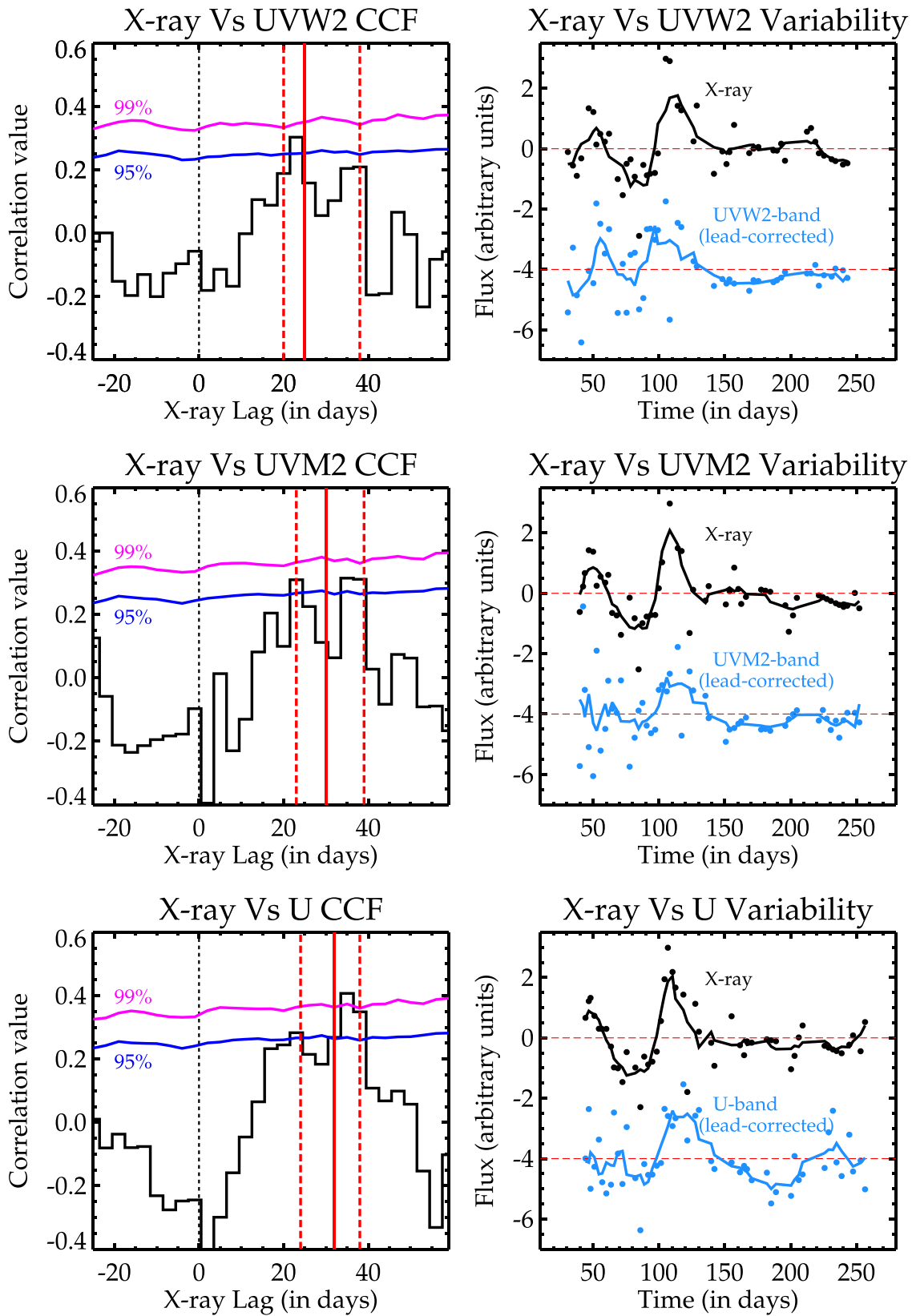
Figure 2. Left panels: X-ray vs. optical/UV cross-correlation functions (CCFs). The two cross-correlated light curves are indicated at the top of each panel. The blue and the magenta curves are the 95% and the 99% confidence contours, respectively. The solid vertical red line is the median of the CCF's centroid distribution, while the dashed vertical lines are the 1σ error bars on the median. These values for the UVW2, UVM2, and the UVW1 ICCFs are 26^{+12}_{-6}, 30^{+8}_{-7}, and 32^{+6}_{-9} days, respectively. Right panels: we compare the variability features in the X-ray light curve (black) with the optical/UV data (blue). The optical/UV light curves were offset by their corresponding lead times. The solid curves are the running average of five neighboring points to guide the eye. Common features in both bands are evident in all the cases.
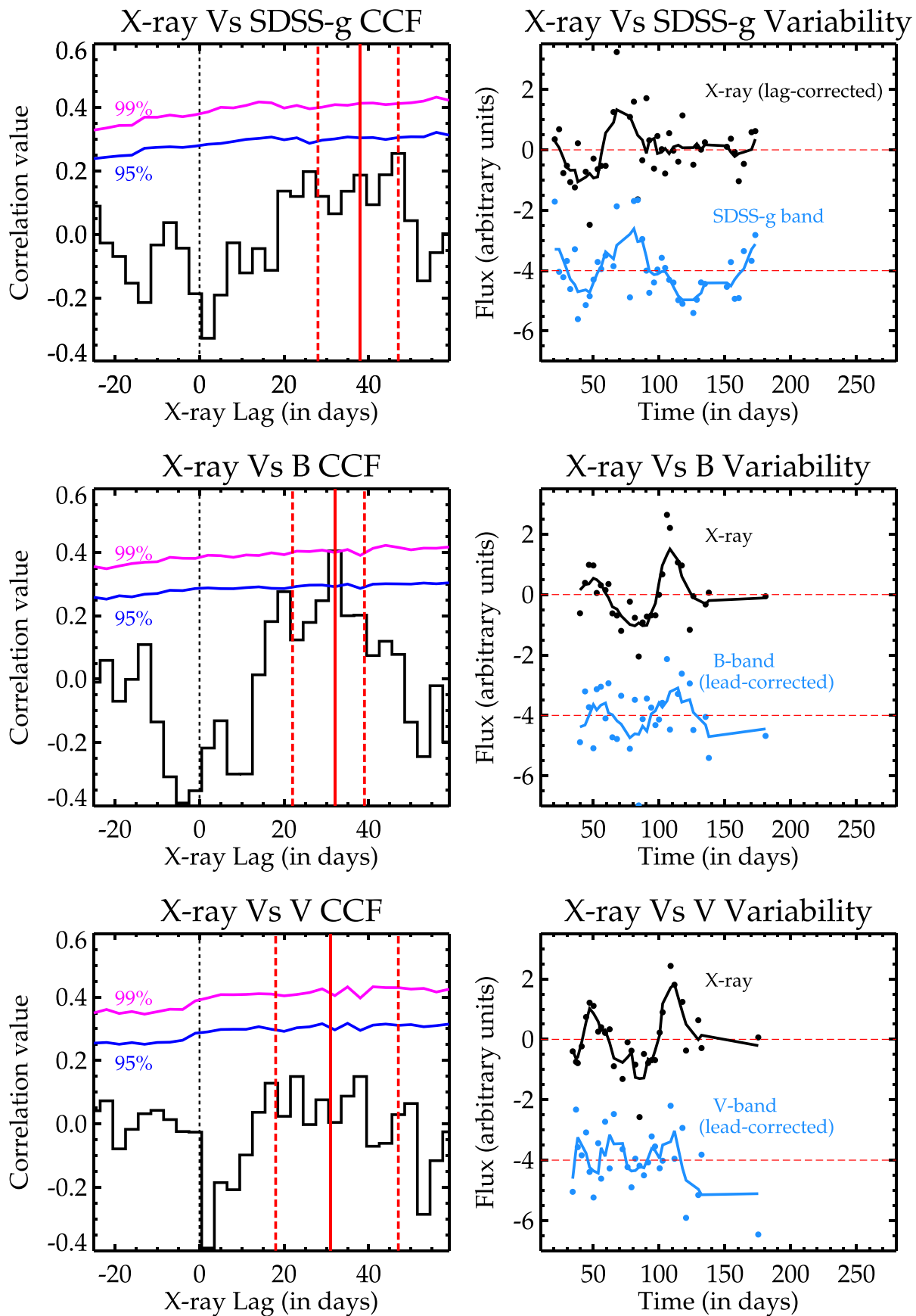
Figure 3. Same as Figure 2, but the median of the CCF's centroid distribution for the SDSS-g, B, and the V band ICCFs are 37^{+9}_{-10}, 32^{+7}_{-10}, and 31^{+16}_{-13} days, respectively. Top right: because the SDSS-g band light curve was better sampled than the X-ray data, we offset the X-ray light curve by the lag implied from the CCF and interpolated the SDSS-g onto the X-ray epochs.

(2) Also, in this scenario, optical/UV fluctuations due to accretion rate perturbations could propagate inward on a timescale corresponding to the local viscous timescale (Arévalo et al. 2008). Then the optical/UV emission leads the X-rays by a few tens to millions of days (Breedt et al. 2009) again depending on the black hole mass and the accretion rate (Shakura & Sunyaev 1973; Figure 3).

It is evident from Figures 1–3 that the optical/UV emission "leads" the X-rays by 32 ± 4 days. This rules out X-ray reprocessing as the dominant source of the variable optical/UV emission. Furthermore, assuming a black hole mass of $10^{6.5 \pm 0.6}$ $M_{\odot}$ as derived from its host galaxy's bulge luminosity and the bulge's stellar velocity dispersion (H16; van Velzen et al. 2016), the seed photon scenario (case (1) above) is also unlikely as it would result in UV lead times of only a few thousands to a few tens of thousands of seconds. Below, we show that direct optical/UV emission from a standard thin disk can also be ruled out.

ASASSN-14li's observed peak bolometric luminosity of roughly 10^{44} erg s^{-1} (H16) implies an accretion rate of $\lesssim 0.2^{+0.7}_{-0.2}$ $\dot{M}_{\rm Edd}$ (where $\dot{M}_{\rm Edd}$ is the Eddington accretion rate). Such a sub-Eddington rate implies that if an accretion disk formed quickly after the disruption it can be described by a geometrically thin, optically thick disk model of Shakura & Sunyaev (1973). The observed lags between the optical, the UV, and the X-ray radiation, if coming from the viscous propagation of accretion rate fluctuations in such a thin disk, require, for possible black hole and disk parameters of ASASSN-14li, that the optical/UV emission come from within a radius of 50 R_g (top left panel of Figure 4; R_g is the gravitational radius). If emitted from outside this radius, the viscous timescales, and therefore the lags, would be much longer than the observed lags. On the other hand, the thin disk around a $10^{6.5 \pm 0.6}$ $M_{\odot}$ black hole of the appropriate luminosity emits most of its optical and UV radiation from outside a radius of 500 R_g (top right panel of Figure 4). As a result, the expected lags due to viscous propagation of perturbation in a thin disk are orders of magnitude longer than the observed ones (bottom panel of Figure 4). This discrepancy rules out the standard, thin, circular disk solution. More importantly, this argues strongly that ASASSN-14li is not an accretion disk-driven AGN flare.

The slim disk accretion disk model (Abramowicz et al. 1988), describing super-Eddington accretion flows, predicts a thicker accretion flow that can produce shorter viscous times comparable with ASASSN-14li's lags. However, ASASSN-14li is sub-Eddington and in this limit the slim disk model reduces to the fiducial thin disk solution (Strubbe & Quataert 2009). Another possibility is that a circular disk of a different nature, thick and very hot (e.g., Coughlin & Begelman 2014), forms. Such a disk can form in principle even for sub-Eddington accretion rates. However, no general solution for such a mode exists, and therefore in this picture the lag magnitude cannot be used to constrain the flow parameters. Finally, a truncated disk model—where the optical/UV are produced by the Rayleigh–Jeans end of an X-ray multi-color blackbody emission—cannot explain the observed high optical/UV luminosities (H16; but see below).

Many recent numerical studies of tidal disruption events (e.g., Guillochon et al. 2014, G14; Shiokawa et al. 2015; Hayasaki et al. 2016; Bonnerot et al. 2017, hereafter B17) have shown that the infalling stellar debris stream will undergo self-interactions because of relativistic apsidal precession (see, for example, Figure 2 of B17). While these studies differ in their predictions

for the evolution of the debris stream following the first self-interaction, they all agree that the role of self-interactions/shocks is to facilitate the process of circularization by removal of angular momentum. For instance, Shiokawa et al. (2015) and P15 argue that following the first stream self-interaction at the apocenter of the most bound debris, material spreads and rushes toward the black hole on the free-fall timescale. On the other hand, B17 suggested a discrete variant of the self-interaction model where the stream undergoes successive self-interactions—without much spreading in each interaction—and can eventually settle into a small ($\sim$ a few tens of gravitational radii) accretion disk. Alternately, the debris can instead lose only a small fraction of its energy in each self-interaction and follow more bound elliptical orbits. This would ultimately lead to the closing of the gap between the apocenter and the black hole, forming an elliptical accretion disk (G14).

The lags of the observed magnitudes can originate in all the three models (see Figure 5 for schematics). In the shock-at-apocenter model, the collisions of streams are likely to result in perturbations of the, otherwise relatively uniform and thin, tidal stream of gas, and subsequently vary the fraction of the tidal debris getting close to the black hole and being trapped or directly accreted there (e.g., Sądowski & Narayan 2015). Such an inner small-scale accretion flow will be hot and will be modulated at the rate at which tidal debris—already affected by the self-interaction at large radii—returns to very close orbits. Therefore, heating up a clump of gas in the dissipation/interaction region resulting in the optical/UV emission will be followed by modulation of the energetic X-ray radiation coming from a region close to the black hole. Furthermore, under such circumstances, X-rays variations are expected to lag the optical/UV fluctuations by the infall time from the stream–stream interaction region. This lag is roughly equal to half the orbital time of the debris orbit. For example, the shortest expected lag in this model would correspond to half the orbital period of the most bound orbit. This is roughly 11 days for a $10^{6.5}$ $M_{\odot}$ black hole (using Equation (4) of P15) and is in agreement with the lags identified in this work. It is also plausible that fluctuations propagate on a thermal timescale that would be slower than the free-fall timescale.

Bonnerot et al. (2017) argue that in the absence of strong magnetic stresses, successive self-interactions can lead to the formation of an inner accretion disk $\sim$a few tens of Rg. Time lags can also manifest in this series-of-discrete-interactions model (see Figure 5). Each stream self-interaction can produce the optical/UV emission similar to the shock-at-apocenter model. Furthermore, fluctuations from the last self-interaction —just before the flow joins the inner accretion disk—can travel down to the black hole on a viscous timescale and modulate the X-rays. The viscous timescale in a thin accretion disk at a radius of a few tens of Rg is comparable to the observed lag (top left panel of Figure 4), and thus suggests that a TDF disk may be confined to within a few tens of Rg.

We can also show that the expected properties of elliptical disks are consistent with the observed lags by constructing a simplistic model following G14. Recent numerical works have shown that the flow can remain elliptical for roughly 10 orbits (B17). Smaller mass black holes can maintain the ellipticity for longer duration. In such a model, we assume the emission follows the same radial profile as in a circular thin disk (Shakura & Sunyaev 1973), but the extent of the emitting region is limited by the size of the elliptical orbit of the most bound gas. Under such assumptions,
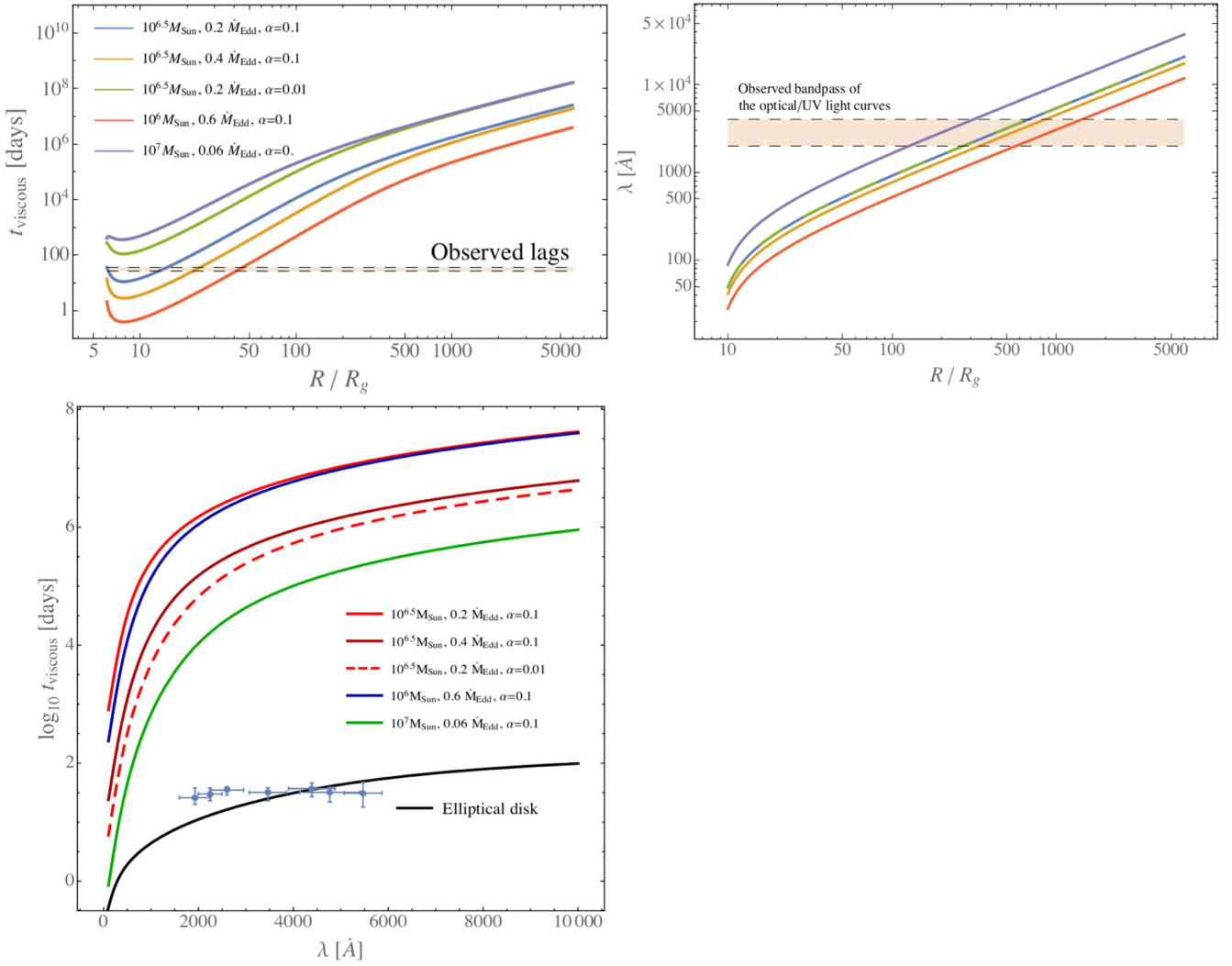
Figure 4. Top: the dependence of viscous timescale (top left) and the wavelength of emission (top right) on the radial distance in a Shakura & Sunyaev (1973) thin disk are shown. The observed lags are inconsistent with a circular thin disk. The solutions for different black hole mass, Eddington ratio, and α-viscosity parameters are shown. Bottom: viscous timescale vs. wavelength of emission for a standard thin disk. The observed time lags, shown as blue data points, are orders of magnitude faster than expected from a circular thin disk. A simplistic elliptical accretion disk model (G14) can reproduce the observed lags and is shown as a black curve.

the radius dominating emission at a given frequency can be approximated as

$$R_\nu = \frac{4\pi \int_{6R_g}^{R_{\max}} R^2 \left(\max\left[1, \frac{R}{2R_T}\right]\right)^{-1} F_{BB}(\nu, T_{eff}(R))\,dR}{4\pi \int_{6R_g}^{R_{\max}} R \left(\max\left[1, \frac{R}{2R_T}\right]\right)^{-1} F_{BB}(\nu, T_{eff}(R))\,dR},$$

where R_T is the tidal radius for $1\,M_\odot$ star and $R_{\max}$ is the apocenter radius for the most bound orbit. $F_{BB}(\nu, T_{eff}(R))$ is the blackbody emission at frequency ν and temperature $T_{eff}(R)$.

To convert the radius at which emission takes place to the lags between given wavelengths and X-rays, we assume that the corresponding viscous timescale is given through $t_{viscous} = \mathcal{V}^{-1} t_{ff}$, where $\mathcal{V}$ is an ad hoc viscosity parameter and t_{ff} is the local free-fall time. In an elliptical disk, this ad hoc viscosity parameter is much higher than in a circular disk because we allow for larger "effective" α-viscosity and disk thickness.

In Figure 4 (bottom panel), we plot the expected lags in the elliptical model as a function of wavelength obtained assuming M_{BH}, black hole mass $= 10^{6.5}\,M_\odot$, accretion rate $= 0.2\dot{M}_{Edd}$, and $\mathcal{V} = 0.05$. The obtained relation fits the observed values of

the lags very well. If the assumed value of $\mathcal{V} = 0.05$ is correct, the gas takes $\sim$20 orbits to spiral down from given radius to the black hole, i.e., the gas would accreted quite rapidly toward the black hole. However, the dynamics of elliptical disks forming in tidal disruption events, and in particular their dissipation and emission profiles, are currently very poorly understood, and thus cannot be used to estimate the flow parameters unambiguously.

In summary, we have presented a cross-correlation analysis that suggests that ASASSN-14li's X-ray variations lag the optical/UV fluctuations by 32 ± 4 days. We propose that at least three models can explain these lags: (1) shocks-at-apocenter model, (2) an elliptical accretion disk model, and (3) series-of-discrete-interactions model. The shocks-at-apocenter model is similar to the model proposed by P15 but, in addition, we propose that the optical and the UV emission originates from physically distinct sites as opposed to the single photosphere scenario suggested by P15. ASASSN-14li's data does not allow us to unambiguously detect the lags between the optical and the UV bands, but high-cadence optical and UV monitoring observations of a TDF would allow us to easily test
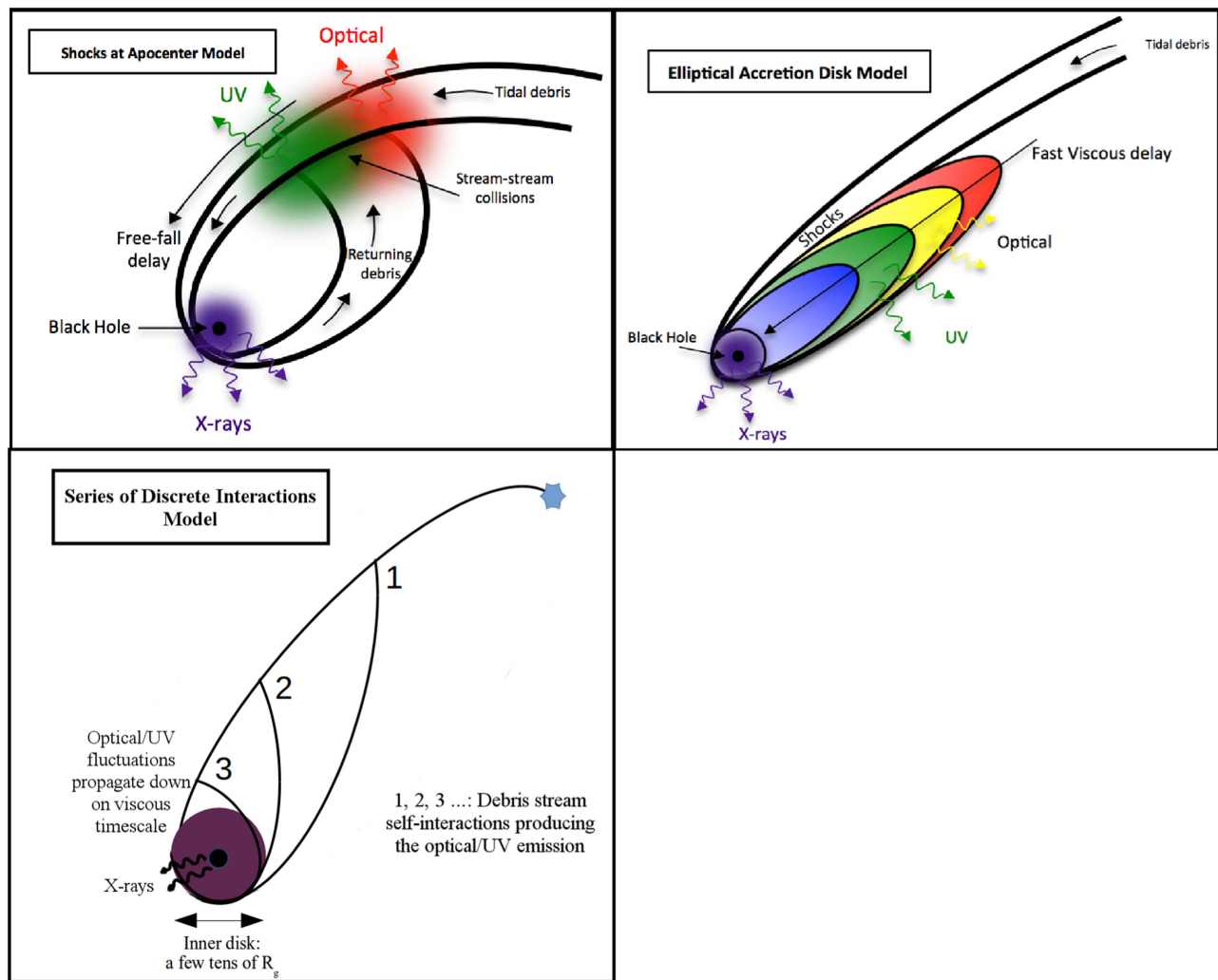
Figure 5. Schematic of the three likely stream self-interaction scenarios for the origin of the optical/UV emission from ASASSN-14li. In the shocks-at-apocenter model (top left), as clumps of debris trace the path shown, they first emit optical radiation, followed by UV and eventually—when near the black hole—modulate the X-rays. The time lag between the emission from these wavebands is dictated by the infall time between the optical, the UV, and the X-ray sites. In the elliptical disk model (top right), the time lags correspond to the local viscous timescale in the disk and are much faster compared to a circular disk of the same radial extent. In the series-of-successive-interactions model (bottom), fluctuations from the last self-interaction can propagate in the inner disk of a few tens of gravitational radii on the viscous timescale (see top left panel of Figure 4).

this hypothesis and establish the origin of the optical/UV emission in other TDFs.

References

Abramowicz, M. A., Czerny, B., Lasota, J. P., & Szuszkiewicz, E. 1988, ApJ, 332, 646
Arévalo, P., Papadakis, I., Kuhlbrodt, B., & Brinkmann, W. 2005, A&A, 430, 435
Arévalo, P., Uttley, P., Kaspi, S., et al. 2008, MNRAS, 389, 1479
Bonnerot, C., Rossi, E. M., & Lodato, G. 2017, MNRAS, 464, 2816
Breedt, E., Arévalo, P., McHardy, I. M., et al. 2009, MNRAS, 394, 427
Breeveld, A. A., Landsman, W., Holland, S. T., et al. 2011, in AIP Conf. Proc. 1358, GAMMA RAY BURSTS 2010 (Melville, NY: AIP), 373
Brown, J. S., W.-S Holoien, T., Auchettl, K., et al. 2017, MNRAS, 466, 4904
Brown, T. M., Baliber, N., Bianco, F. B., et al. 2013, PASP, 125, 1031
Burrows, D. N., Hill, J. E., Nousek, J. A., et al. 2005, SSRv, 120, 165
Chornock, R., Berger, E., Gezari, S., et al. 2014, ApJ, 780, 44
Coughlin, E. R., & Begelman, M. C. 2014, ApJ, 781, 82
Dai, L., McKinney, J. C., & Miller, M. C. 2015, ApJL, 812, L39
Edelson, R., Gelbord, J. M., Horne, K., et al. 2015, ApJ, 806, 129
Edelson, R. A., & Krolik, J. H. 1988, ApJ, 333, 646
Gandhi, P., Dhillon, V. S., Durant, M., et al. 2010, MNRAS, 407, 2166
Gehrels, N., Chincarini, G., Giommi, P., et al. 2004, ApJ, 611, 1005
Guillochon, J., Manukian, H., & Ramirez-Ruiz, E. 2014, ApJ, 783, 23
Hayasaki, K., Stone, N., & Loeb, A. 2016, MNRAS, 461, 3760
Hills, J. G. 1975, Natur, 254, 295
Holoien, T. W.-S., Kochanek, C. S., Prieto, J. L., et al. 2016a, MNRAS, 455, 2918
Holoien, T. W.-S., Kochanek, C. S., Prieto, J. L., et al. 2016b, MNRAS, 463, 3813
McHardy, I. M., Connolly, S. D., Peterson, B. M., et al. 2016, AN, 337, 500
Miller, J. M., Kaastra, J. S., Miller, M. C., et al. 2015, Natur, 526, 542
Morgan, C. W., Kochanek, C. S., Morgan, N. D., & Falco, E. E. 2010, ApJ, 712, 1129

Pasham et al.

Pasham, D. R., Cenko, S. B., Zoghbi, A., et al. 2015, ApJL, 811, L11
Peterson, B. M., Ferrarese, L., Gilbert, K. M., et al. 2004, ApJ, 613, 682
Peterson, B. M., Wanders, I., Bertram, R., et al. 1998, ApJ, 501, 82
Piran, T., Svirski, G., Krolik, J., Cheng, R. M., & Shiokawa, H. 2015, ApJ,
    806, 164
Poole, T. S., Breeveld, A. A., Page, M. J., et al. 2008, MNRAS, 383, 627
Rees, M. J. 1988, Natur, 333, 523
Reynolds, C. S., & Nowak, M. A. 2003, PhR, 377, 389
Roming, P. W. A., Kennedy, T. E., Mason, K. O., et al. 2005, SSRv, 120, 95

Roth, N., Kasen, D., Guillochon, J., & Ramirez-Ruiz, E. 2016, ApJ, 827, 3
Sądowski, A., & Narayan, R. 2015, MNRAS, 453, 3213
Shakura, N. I., & Sunyaev, R. A. 1973, A&A, 24, 337
Shappee, B. J., Prieto, J. L., Grupe, D., et al. 2014, ApJ, 788, 48
Shiokawa, H., Krolik, J. H., Cheng, R. M., Piran, T., & Noble, S. C. 2015, ApJ,
    804, 85
Strubbe, L. E., & Quataert, E. 2009, MNRAS, 400, 2070
Tombesi, F., Cappi, M., Reeves, J. N., et al. 2010, A&A, 521, A57
van Velzen, S., Anderson, G. E., Stone, N. C., et al. 2016, Sci, 351, 62